Research on strategies to improve the corrosion resistance of metal surface coatings in low-temperature corrosive environments

Alex David[1]

[1]Manchester Metropolitan University, United Kingdom

***Corresponding Author:**
dalexjohn@gmail.com

Received: 21/12/2024
Revised: 10/02/2025
Accepted: 11/06/2025
Published: 30/06/2025

Abstract: The advancement of polar marine engineering has led to increasing demands on the performance of metal coatings. This paper aims to enhance the corrosion resistance of metal surface coatings by modifying epoxy resin using thiazole-graphene oxide (AMT-GO) and a curing agent. Combining coating processes and curing techniques, the metal surface coating is successfully applied. Through various types of testing, the improved corrosion resistance of the organic coating (AMT-GO/EP) is evaluated. The research results show that in different tests, the AMT-GO/EP coating exhibits fewer than 10 chemical composition shift peaks. Adhesion decreases by only 17.79%. At room temperature, the maximum corrosion potential is -0.27 V, and the minimum corrosion current density is -8.56 A/cm^2. At room temperature in saltwater, the potential positive shift was only 0.05V, and the current density was also lower than that of other coatings. The coating exhibited the strongest resistance performance in ultra-low-temperature saltwater.

Keywords: modified epoxy resin, metal coating, AMT-GO/EP, corrosion resistance

1 | Introduction

With the development of industrial construction in high-altitude cold regions, the corrosion resistance of metal materials exposed to low-temperature environments has become a serious issue. Low-temperature corrosion is a common form of metal corrosion that primarily occurs in low-temperature environments, such as liquid nitrogen and liquid oxygen [1]. The underlying principle is that at low temperatures, the metal surface reacts chemically with surrounding gases or liquids, leading to corrosion and damage on the metal surface. This is a significant issue in many industrial sectors, particularly in petrochemicals, aerospace, and nuclear industries [2, 3, 4]. At low temperatures, chemical reaction rates are slower, preventing the rapid formation of a protective layer on the metal surface. This leaves the metal surface exposed to chemical substances, making it susceptible to erosion and damage [5, 6]. Additionally, in low-temperature environments, the crystal structure of metals undergoes phase transitions, resulting in an increase in lattice constants and making the crystals more brittle. This makes metal materials more susceptible to stress concentration and crack propagation. These cracks and fractures not only weaken the strength and toughness of metal materials but also provide more opportunities for chemical substances to penetrate into the metal interior, thereby exacerbating the severity of low-temperature

corrosion [7, 8, 9]. Furthermore, low-temperature corrosion environments alter the surface properties and chemical composition of metal materials, affecting material performance such as conductivity and magnetic properties. This leads to corrosion and damage on the metal surface, reducing material strength and toughness, impacting material service life and safety, and causing failures and damage to related metal equipment, thereby affecting production and work efficiency [10, 11, 12, 13]. Therefore, the corrosion resistance of metal surface coatings in low-temperature corrosion environments is particularly important.

In low-temperature environments, the performance of coatings is often significantly affected, presenting a series of challenges for their application in relevant fields. At low temperatures, the evaporation rate of solvents in coatings slows down, and the reactivity of resins decreases, resulting in significantly prolonged drying and curing times for coatings; coating films become more brittle, and ice crystal formation can lead to cracking and peeling issues, thereby reducing the protective performance of coatings [14, 15, 16, 17]. Additionally, under low-temperature conditions, the viscosity of coatings increases, their flowability decreases, and the rate of electrochemical corrosion slows down. However, as temperatures drop into ultra-low-temperature environments, the corrosion rate accelerates [18, 19]. To address this, researchers have proposed various solutions to enhance the corrosion resistance of metal surface coatings.

Sun et al. [20] modified FeO_4 nanoparticles using glycidyl methacrylate and incorporated them into an epoxy coating, which exhibited excellent corrosion resistance. Arthanareeswari et al. [21] developed a low-temperature composite coating of nano-titanium dioxide and nano-zinc phosphate for low-carbon steel, with a nano-titanium dioxide addition of 1.0 g/L yielding the optimal corrosion resistance for the composite coating. Xie et al. [22] found that the addition of graphene oxide not only enhances the phosphating rate of low-temperature phosphate coatings but also improves their corrosion resistance. Zhu et al. [23] developed a polypyrrole-functionalized graphene oxide nanocomposite and incorporated it into phosphate coatings, significantly improving the corrosion resistance of the coatings, with optimal performance achieved at a concentration of 1.2 g/L. Shi et al. [24] prepared a chromium-myristic acid mixture superhydrophobic coating with low-temperature dew point corrosion resistance using an electrodeposition method, which significantly enhanced the corrosion resistance of the 09CrCuSb steel substrate. Zhu et al. [25] modified negatively expanded graphene using silane coupling agents and used it as a filler for an epoxy resin coating. Under ultra-low temperature conditions of -196°C, the coating inhibited electrochemical corrosion on the metal surface and improved the coating's corrosion resistance. Zhang et al. [26] proposed a polyvinyl alcohol-polyvinylidene fluoride-fluoromontmorillonite composite material multi-level rough superhydrophobic coating suitable for marine environments. When applied to aluminum alloy surfaces, it significantly improved corrosion resistance, anti-icing performance, and also exhibited good drag-reducing performance and stability. Zhu et al. [27] tested the corrosion resistance of spherical tungsten boride cobalt-based coatings on EH40 steel substrates under low-temperature conditions. As the tungsten boride content increased, the coating's corrosion resistance first increased and then decreased. Wang et al. [28] designed a tungsten carbide-nickel-based coating for EH40 steel. At -40°C, the 15% tungsten carbide coating exhibited the lowest corrosion current and strong corrosion resistance. Additionally, as the demand for low-temperature coating corrosion resistance has surged, the self-healing functionality of coatings has gained significant attention. Kim et al. [29] shared a microcapsule coating made from the polymerization of polydimethylsiloxane and dibutyldioctanoate, which has low-temperature self-healing functionality and passed scratch and corrosion tests.

To address the issue of metal surface coatings being prone to corrosion, this paper proposes a technical improvement framework using thiazole (AMT) and graphene oxide (GO) for epoxy resin modification. AMT-GO was prepared in the laboratory and combined with a curing agent to coat metal steel plates, completing the

preparation of AMT-GO/EP organic coating samples. Comprehensive surface performance and corrosion resistance tests were conducted on the coating samples, combined with characterization analysis, to systematically compare the synthesis effectiveness of the prepared samples and the efficacy of the proposed strategy.

2 | Analysis of corrosion resistance testing and testing methods for metal coatings

2.1 | Test preparation

2.1.1 | Preparation of AMT-GO

The raw materials are 2-amino-5-mercapto-1,3,4-thiadiazole (AMT) and graphene oxide (GO). The preparation steps for thiadiazole-graphene oxide (AMT-GO) are as follows: Take 0.25 g of GO and add it to 150 mL of anhydrous ethanol to obtain a GO dispersion solution with a concentration of 2.5 mg/mL, then stir and sonicate for 10 minutes; Add 0.25 g of AMT to the GO dispersion solution and sonicate for 10 minutes to ensure uniform dispersion; Use a magnetic stirrer to stir the dispersion solution at 50°C for 48 hours to obtain the AMT-GO solution; Then wash with pure water seven times, centrifuge, dry, and grind to obtain black-brown AMT-GO powder.

Chemical structure analysis of the powder samples of GO, AMT, and AMT-GO was performed using Fourier transform infrared spectroscopy (FT-IR) and X-ray photoelectron spectroscopy (XPS) to determine whether the experimental reaction mechanism successfully synthesized AMT-GO. Scanning electron microscopy (SEM), transmission electron microscopy (TEM), and atomic force microscopy (AFM) were used to further characterize the microstructure and thickness of GO and AMT-GO, indicating that AMT-GO has a large interlayer spacing and good dispersion.

2.1.2 | Preparation of organic coatings

The raw materials are epoxy resin E44, curing agent T31, and xylene. Q235 steel plates are sanded with 240-grit and 400-grit sandpaper, then ultrasonically cleaned in an ethanol solution before use. Taking the AMT-GO/EP composite coating as an example: 5 g of epoxy resin was weighed, diluted with 2 g of xylene solvent, and thoroughly stirred; then 0.02 g of AMT-GO nano-filler was added, ultrasonicated and stirred for 35 minutes, followed by the addition of 2 g of T31 hardener, ultrasonicated and stirred for 15 minutes, and vacuum degassed for 35 minutes to obtain AMT-GO-modified epoxy resin; Subsequently, the epoxy resin was uniformly applied to the cleaned Q235 steel plate using a wire rod applicator, cured at -15°C in a refrigerator for 48 hours, yielding a low-temperature cured AMT-GO-modified epoxy coating (AMT-GO/EP). Additionally, low-temperature cured pure epoxy coating (EP) and graphene-modified epoxy coating (GO/EP) were prepared as controls, with coating thicknesses of (75±10) μm.

2.2 | Coating surface performance testing methods

Regular testing and analysis of coating samples mainly includes the following six types.

2.2.1 | Electrochemical impedance testing

The instrument used for electrochemical impedance spectroscopy (EIS) testing is an electrochemical workstation model PARSTAT2273. The three-electrode system used for testing consists of a coated sample (working electrode, test area 25 cm^2), a saturated calomel electrode (reference electrode), and a platinum electrode (counter electrode). The test solution is a 4.0% NaCl solution. The frequency range is set from 10^{-3}Hz∼10^6 Hz, with 45 test frequency points selected, and the signal amplitude is set to 0.05 V.

2.2.2 | Open circuit potential monitoring

Use the MAS830L multimeter to test the open circuit potential (OCP) of the coated sample. The test solution is 4.0% NaCl. Connect the coated sample to the positive terminal and the reference electrode to the negative terminal. Set the multimeter to voltage test mode and select the appropriate range. Immerse the sample in the test solution and record the value once the reading stabilizes.

2.2.3 | Adhesion test

After the test has been conducted for a certain period of time, the coated samples are removed and left to dry at room temperature for 3 hours. Eight aluminum columns are then uniformly attached to the coated surface using Ergo 1690 adhesive. During bonding, each column must be spaced at a certain distance from the others. After bonding is complete, a weight of approximately 2.5 kg is placed on the aluminum columns to ensure that the adhesive comes into full contact with the coating surface, making the bond more secure. The samples are then left at room temperature for 48 hours. Finally, an adhesion tester was used to perform a pull-off test on the aluminum columns. Before testing adhesion, the coating around the aluminum columns was scraped off using the adhesion tester's accessories to expose the metal substrate, ensuring that the adhesion being tested was that of the adhesive bonding area. The test results were then recorded.

2.2.4 | Gloss and color difference testing

Regular measurements of the gloss of the coating are taken using a gloss meter. During testing, three parallel positions on the sample surface are selected for testing, and the average value of the results is taken. To ensure accuracy, the same positions should be selected as much as possible for each test. Calculate the gloss loss rate of the coating using Eq. (1), where A_0 and A_t represent the initial gloss of the coating before the experiment and the gloss at time t, respectively.

$$Glossloss/\% = \frac{A_0 - A_t}{A_0} \cdot 100.0\%. \tag{1}$$

Use a portable color difference meter to regularly test the color difference of the coating. During testing, select three uniform positions on the sample surface for testing and calculate the average value. To ensure accuracy, the same positions should be selected as much as possible each time testing is performed. Calculate the color difference value (ΔE^*_{ab}) of the coating using Eq. (2). Every color has corresponding coordinate values, where L, a, and b represent the colorimetric values of the object's color, i.e., the color space coordinates of that color. L represents lightness; a represents red-green chromaticity; and b represents yellow-blue chromaticity.

ΔL, Δa, and Δb indicate the changes in colorimetric values in the corresponding directions.

$$\Delta E^*_{ab} = \sqrt{(\Delta L^*)^2 + (\Delta a^*)^2 + (\Delta b^*)^2}. \quad (2)$$

2.2.5 | Fourier infrared spectroscopy testing

Chemical composition of organic coatings is analyzed using Fourier transform infrared spectroscopy. Prior to each sampling, background data is collected first. A clean blade is then used to scrape and collect a small amount (approximately 1.5 mg) of coating powder from the test surface of the coating sample. Mix the coating powder with potassium bromide particles (analytical grade, 99%) and grind thoroughly. Prepare the sample using the tableting method. After testing, the obtained data must be processed, including baseline correction and normalization.

2.2.6 | Scanning electron microscopy and component analysis

Scanning electron microscopy (SEM) was used to observe the microstructure of the coating surface and the corrosion condition of the substrate beneath the coating. An X-ray energy dispersive spectrometer (EDS) was employed to analyze the composition of the coating and substrate surfaces. Prior to testing, the coating surface was thoroughly cleaned with deionized water and anhydrous ethanol to ensure it was free of contaminants. To observe the corrosion condition of the substrate beneath the coating, the coating samples were first immersed in a paint remover (mainly composed of N,N-dimethylformamide solution) for 48 hours to remove the organic coating and expose the substrate metal. The substrate surface was then cleaned repeatedly with deionized water and ethanol and dried.

2.3 | Coating corrosion resistance test method

2.3.1 | Neutral salt spray test

The Neutral Salt Spray Test (NSS) is one of the most commonly used methods for evaluating the corrosion resistance of metals and coatings. In this experiment, a salt spray test chamber was selected for the testing.

Before the experiment, the test samples were placed inside the salt spray test chamber, with the test surface facing upward at an angle of 25±10° relative to the vertical line. Care should be taken to avoid contact between test samples to prevent liquid accumulation during the test, which could affect test accuracy. Distilled water was added to the test chamber to maintain the temperature and humidity during the test. A sodium chloride solution with a concentration of 60±5 g/L was prepared for the salt spray test chamber, and its pH was maintained between 6.50 and 7.20. The temperature inside the test chamber was controlled to 40°C via the test chamber control panel, and the experiment was initiated and timed.

During the experiment, the test samples were inspected every 48 hours to check for red rust. If red rust appeared, the experiment was terminated.

2.3.2 | Saltwater immersion test

The saltwater immersion test can assess the long-term corrosion resistance of coatings and is the simplest of the three corrosion testing methods. After preparing a 4.0% sodium chloride solution at room temperature, the test samples are vertically immersed in the solution, ensuring that the upper edge of the sample is at least 2.5 cm above the liquid surface and does not come into contact with the container. Once all test samples are at the same height, the container is sealed, and the test begins. During the test, the saltwater is replaced every 7 days, while observing the condition of the coating and recording the corrosion status of the coating and the test duration.

2.3.3 | Ultra-low temperature durability test

To test and evaluate the stability and corrosion resistance of the coating after frequent temperature drops, the coating was placed in an 85°C oven for 10 minutes, then quickly placed in a thermos filled with liquid nitrogen for 10 minutes of ultra-low temperature freezing. This process was repeated 6, 12, 18, and 24 times. The coating was observed for any damage, and the process was stopped upon detection of damage, thereby determining the coating's stability under frequent ultra-low-temperature freezing. Using an Autolab PGSTAT302N electrochemical workstation, electrochemical AC impedance testing was conducted on the coating to assess changes in its corrosion resistance after undergoing a specific number of extreme temperature cycles. The testing electrode system employed a traditional three-electrode configuration, with carbon steel protected by the coating as the working electrode, a carbon rod as the counter electrode, and an Ag/AgCl electrode as the reference electrode. Testing was conducted in a 4.0% NaCl solution. During the test, the AC voltage frequency was gradually reduced from 10^6 Hz to 10^{-3} Hz to obtain the capacitive and resistive characteristics of the coating. The amplitude of the AC voltage was 25 mV.

3 | Comparison and analysis of coating performance test and characterization results

3.1 | AMT-GO chemical structure analysis

Figure 1 shows the chemical structures of GO, AMT, and AMT-GO powder samples under FT-IR and XPS. Before dispersion and mixing, the absorption peaks of graphene oxide (GO) and thiadiazole (AMT) appear closer to 4500 cm^{-1}. After mixing and preparation, the absorption peaks of thiadiazole-graphene oxide (AMT-GO) shift toward 500 cm^{-1}. This is primarily due to the reaction of corresponding groups between GO and AMT, resulting in stretching vibrations of the secondary amine group (-NH-). This indicates that the amine groups in AMT have been successfully grafted onto the graphene surface, confirming the successful synthesis of the composite coating.

3.2 | Analysis of the microstructure and thickness of organic coatings

3.2.1 | Scanning of the microstructure of organic coatings

After uniformly applying the synthetic coating to the steel plate and curing it, the AMT-GO/EP organic composite coating used in the experiment was obtained. A microscopic three-dimensional morphology scan

was performed on the AMT-GO-modified epoxy coating with 0.02 g of AMT-GO nanofiller added and the as-prepared state. Figure 2 shows the microscopic three-dimensional morphology scan results of the AMT-GO-modified epoxy coating. Figure 3 shows the microscopic three-dimensional morphology scanning results of the final prepared organic composite coating. After adding the curing agent and performing a series of curing operations, the organic composite coating exhibited better dispersion of the maximum height difference (ΔZ) on the coating surface in both the horizontal and vertical directions compared to the original AMT-GO-modified epoxy coating. Specifically, in the horizontal direction, the number of microscopic peaks increased by an order of magnitude within the 0.0–3.0 mm length range; in the vertical direction, the number of microscopic peaks also increased by an order of magnitude within the 0.0–2.0 mm length range. This is because, after curing, the coating provides more uniform protection for the metal steel plate.

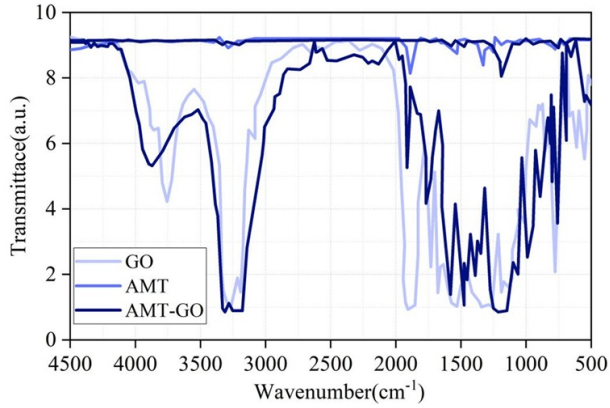

FIGURE 1 Chemical structures of the powder samples of GO, AMT, and AMT-GO

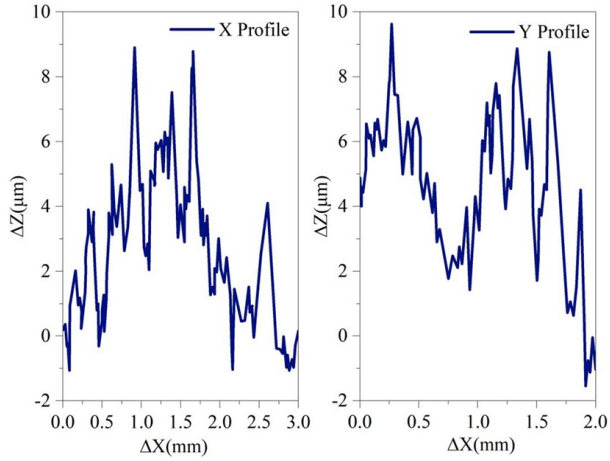

FIGURE 2 Three-dimensional morphology of AMT-GO modified epoxy coating

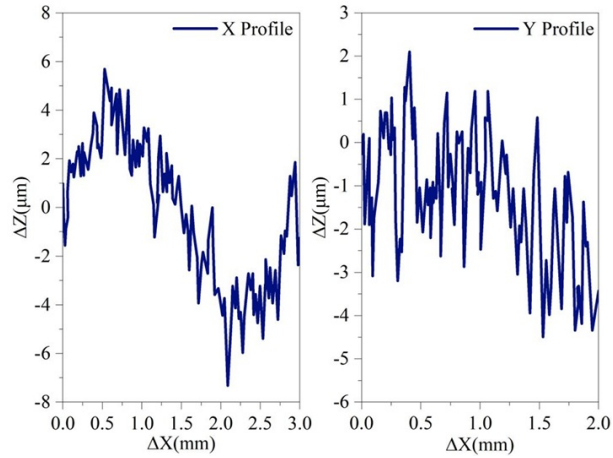

FIGURE 3 Final preparation of the three-dimensional morphology of the coating

3.2.2 | Comparison of microstructures of different coatings

Further scanning of the microstructure of pure epoxy coating (EP) and graphene-modified epoxy coating (GO/EP) was conducted, with the horizontal direction as an example, to compare their dispersion differences with AMT-GO/EP. Figure 4 shows the microstructure of EP and GO/EP in the horizontal direction. In the horizontal direction, the maximum height difference of both comparison coatings is within the range of [-6,6] μm, with a dispersion range smaller than that of AMT-GO/EP ([-8,8] μm), and more significant fluctuations within the horizontal range of 0.0–3.0 mm. This indicates that in terms of dispersion, EP and GO/EP are inferior to AMT-GO/EP.

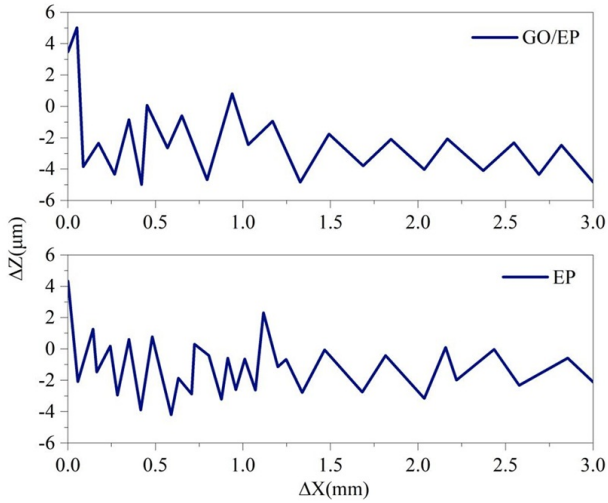

FIGURE 4 Microscopic morphology of EP and GO/EP in the horizontal direction

3.3 | Testing and characterization of different organic coatings

3.3.1 | Fourier infrared spectroscopy comparison

During the experiment, the chemical composition of different organic coatings was collected multiple times and subjected to Fourier transform infrared spectroscopy (FTIR) testing to analyze changes in chemical composition during the erosion process, thereby assessing the protective efficacy of the coatings on the metal substrate. Figure 5 shows the FT-IR test results for EP, GO/EP, and AMT-GO/EP. Within the wavenumber range of 4500 cm^{-1} to 500 cm^{-1}, the chemical compositions of the three different coatings exhibited varying numbers of peak fluctuations within the maximum height difference range of [-8,8] μm. Comparing the number of peak fluctuations, AMT-GO/EP exhibits fewer peaks, not exceeding 10, with overall fluctuations being smoother compared to EP and GO/EP. This demonstrates that during corrosion resistance testing, the chemical composition changes of the AMT-GO/EP organic coating are smaller, i.e., closer to the original coating composition, resulting in lighter corrosion severity.

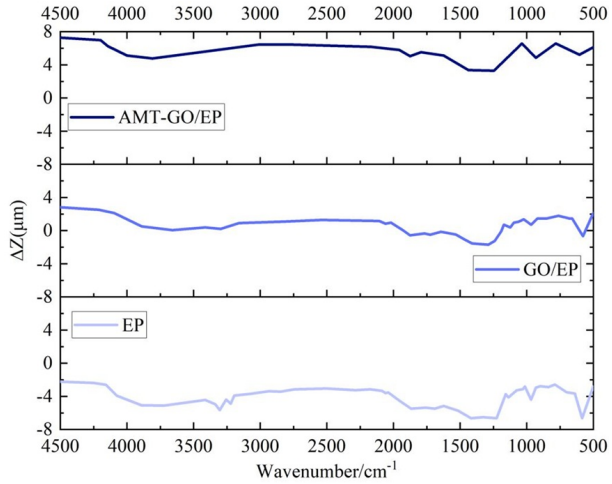

FIGURE 5 FT-IR of EP, GO/EP, and AMT-GO/EP

3.3.2 | Adhesion comparison

Figure 6 shows the changes in adhesion of three different coatings during the experiment. Over the 48-hour adhesion test period, the adhesion of the AMT-GO/EP organic coating decreased from a high of 91.74% to 73.95%, the GO/EP coating adhesion decreased from 91.32% to 28.59%, and the EP coating adhesion decreased from 91.12% to 17.36%. The change in adhesion strength of the AMT-GO/EP organic coating was only a decrease of 17.79%, significantly lower than the 62.73% and 73.76% decreases observed in the comparison coatings. Therefore, the AMT-GO/EP organic coating exhibits superior adhesion strength in corrosive environments, enabling it to adhere more effectively to metal surfaces and enhance metal protection performance.

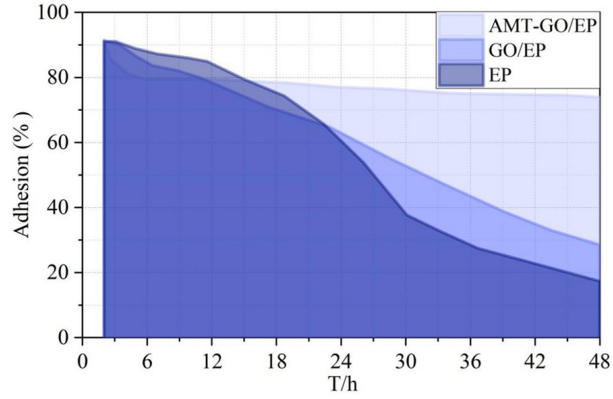

FIGURE 6 The adhesion changes of three different coatings

3.3.3 | Analysis of polarization performance at room temperature

The corrosion potential (E_{corr}, V) and corrosion current density (i_{corr}, A/cm^2) of each sample were determined using electrochemical analysis software. Generally, lower i_{corr} and higher E_{corr} indicate better corrosion resistance of the sample. Figure 7 shows the dynamic potential polarization curves of Q235 steel plates and three coated samples at room temperature (controlled at 40°C in the experimental chamber). Compared to bare Q235 steel, the i_{corr} values of all coatings were significantly reduced, and the E_{corr} values were higher, indicating that the coatings provide effective protective capabilities. Clearly, the AMT-GO/EP coating exhibits the highest E_{corr} (-0.27 V) and the lowest i_{corr} (-8.56 A/cm^2). The addition of AMT-GO coating further enhances the corrosion resistance of the AMT-GO/EP coating at room temperature, providing better protection for the metal.

3.3.4 | Comparison of polarization performance in room temperature salt water

Figure 8 shows the changes in self-corrosion potential and self-corrosion current density over time for the three coatings immersed in saltwater at room temperature for 14 days. It can be observed that, as time progresses, the potentials of all three coatings exhibit a positive shift. Under the same conditions, the more positive the potential, the greater the inertness of the coating. The potential shift for AMT-GO/EP is 0.05 V, for GO/EP it is 0.15 V, and for EP it is 0.3 V. AMT-GO/EP has the smallest potential shift, the lowest corrosion rate, and the current density remains the lowest throughout the time period. This indicates that the AMT-GO/EP coating exhibits the best corrosion resistance polarization performance in room-temperature saltwater.

3.3.5 | Analysis of resistance performance in ultra-low temperature brine

Figure 9 shows the impedance spectra of the three coatings after immersion in ultra-low temperature salt water at [-85°C, 85°C]. The larger the arc, the stronger the corrosion resistance of the coating. After undergoing multiple rapid temperature drops in ultra-low temperature durability testing, the AMT-GO/EP coating exhibited the largest arc, with values approaching 0–20 $\times$ 10^{-3} $\Omega \cdot cm^2$ in the horizontal direction and 0–8 $\times$ 10^{-3} $\Omega \cdot cm^2$ in the vertical direction. Additionally, the amplitude of the arc fluctuations remained very small

under rapid temperature changes. This indicates that the AMT-GO/EP coating exhibits superior impedance performance in ultra-low-temperature saltwater compared to the reference coating, providing stronger protective effects on metal surfaces.

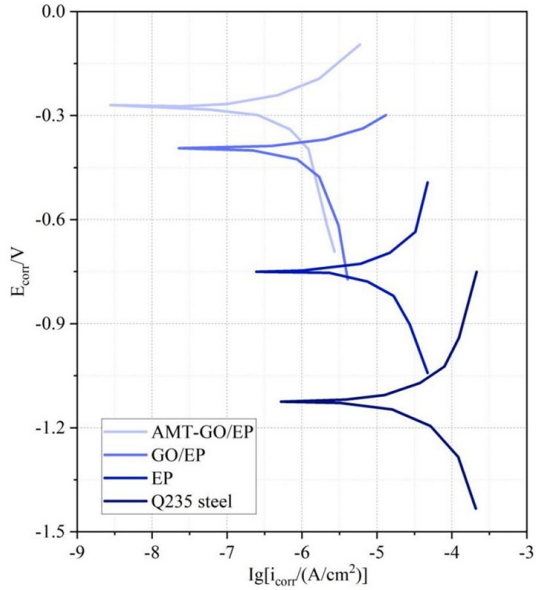

FIGURE 7 Polarization curves of Q235 steel and 3 of waterborne epoxy resin coatings

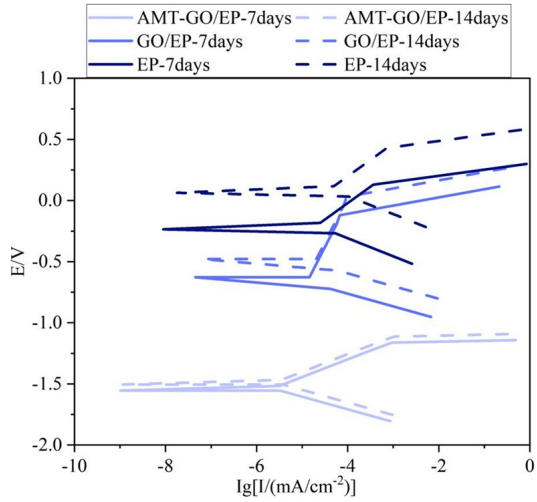

FIGURE 8 Polarization properties of 3 coatings in room-temperature saline

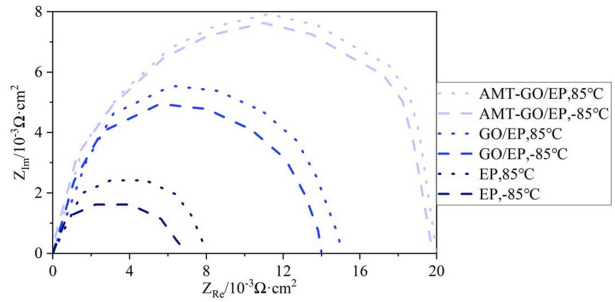

FIGURE 9 Impedance spectra after ultra-low-temperature immersion of 3 coatings

4 | Conclusion

This paper uses AMT-GO modified epoxy resin to improve the corrosion resistance of metal surface coatings. AMT-GO/EP exhibits a more dispersed distribution of maximum height differences in the horizontal direction (0.0–3.0 mm) and vertical direction (0.0–2.0 mm), with superior dispersion performance compared to the control coating. Within the maximum height difference range of [-8, 8] μm, the number of chemical composition peaks in AMT-GO/EP is less than 10. In a 48-hour test, adhesion decreased from 91.74% to 73.95%. At 40°C room temperature, E_{corr} reached a maximum of -0.27 V, and i_{corr} reached a minimum of -8.56 A/cm^2. Under room temperature saltwater test conditions, the potential displacement was 0.05 V, lower than the 0.15 V and 0.3 V of the comparison coating. In the low-temperature durability test from -85°C to 85°C, the AMT-GO/EP coating exhibited a circular arc range of 0–20 $\times$ 10^{-3} $\Omega \cdot cm^2$ (horizontal direction) and approximately 0–8 $\times$ 10^{-3} $\Omega \cdot cm^2$ (vertical direction), demonstrating optimal resistance performance.

References

[1] Zhang, Q., Sun, F., & Chen, C. (2019). Research on the three-dimensional wall temperature distribution and low-temperature corrosion of quad-sectional air preheater in larger power plant boilers. *International Journal of Heat and Mass Transfer, 128*, 739-747.

[2] Wen, Y. H., Liu, J. J., Li, L. T., Li, Y., Leng, W. J., Feng, L., & Cui, Z. Y. (2025). Understanding corrosion behavior of Q420 steel in low temperature environment with freezing–thawing cycling: YH Wen et al. *Journal of Iron and Steel Research International*, 1-18.

[3] Choi, Y. Y., & Kim, M. H. (2018). Corrosion behaviour of welded low-carbon steel in the Arctic marine environment. *RSC Advances, 8*(53), 30155-30162.

[4] Shi, X. Z., Cui, Z. Y., Li, J., Hu, B. C., An, Y. Q., Wang, X., & Cui, H. Z. (2023). Atmospheric corrosion of AZ31B magnesium alloy in the Antarctic low-temperature environment. *Acta Metallurgica Sinica (English Letters), 36*(9), 1421-1432.

[5] Borgioli, F. (2023). The corrosion behavior in different environments of austenitic stainless steels subjected to thermochemical surface treatments at low temperatures: an overview. *Metals, 13*(4), 776.

[6] Milovanović, N., Đorđević, B. R., Tatić, U., Sedmak, S., & Strbacki, S. (2017). Low-temperature corrosion damage and repair of boiler bottom panel tubes. *Structural Integrity and Life, 17*(2), 125-131.

[7] Zhao, W., Feng, G., Zhang, M., Ren, H., & Sinsabvarodom, C. (2020). Effect of low temperature on fatigue crack propagation rates of DH36 steel and its butt weld. *Ocean Engineering, 196*, 106803.

[8] Peng, Y., Chen, C., Li, X., Gong, J., Jiang, Y., & Liu, Z. (2017). Effect of low-temperature surface carburization on stress corrosion cracking of AISI 304 austenitic stainless steel. *Surface and Coatings Technology, 328*, 420-427.

[9] Pan, C., Cui, Y., Liu, L., Guo, M., & Wang, Z. (2020). Effect of temperature on corrosion behavior of low-alloy steel exposed to a simulated marine atmospheric environment. *Journal of Materials Engineering and Performance, 29*(2), 1400-1409.

[10] Jing, J. Q., Guo, J., Li, B., Jia, S. J., & Ren, Y. (2021). Relationship between microstructure and corrosion behavior of high-grade pipeline steel in a low-temperature environment. *Journal of Iron and Steel Research International, 28*(8), 1037-1046.

[11] Yang, G., Xu, C., Zhang, J., Liu, C., Cui, H., Zeng, L., ... & Li, X. (2024). Effect of dissolved oxygen on corrosion behavior and mechanism of X70 pipeline steel in simulated low temperature bentonite-containing alkaline chloride environment. *Construction and Building Materials, 438*, 137170.

[12] Rajput, A., Park, J. H., Hwan Noh, S., & Kee Paik, J. (2020). Fresh and sea water immersion corrosion testing on marine structural steel at low temperature. *Ships and Offshore Structures, 15*(6), 661-669.

[13] Liu, H., Zhou, Y., Wang, F., Lu, Y., & Chen, Z. (2024). Experimental study on impact toughness of structural steel and its butt-welded joint at low temperature and corrosion. *Journal of Constructional Steel Research, 212*, 108298.

[14] Lee, K., Kang, J., Lee, J., Lee, S., & Bae, J. (2018). Evaluation of metal-supported solid oxide fuel cells (MS-SOFCs) fabricated at low temperature ($\sim$ 1,000° C) using wet chemical coating processes and a catalyst wet impregnation method. *International Journal of Hydrogen Energy, 43*(7), 3786-3796.

[15] Man, C., Wang, Y., Li, W., Kong, D., Yao, J., Grothe, H., ... & Dong, C. (2021). The anti-corrosion performance of the epoxy coating enhanced via 5-Amino-1, 3, 4-thiadiazole-2-thiol grafted graphene oxide at ambient and low temperatures. *Progress in Organic Coatings, 159*, 106441.

[16] Wang, X. Y., Wang, S., Su, J. F., Shao, R. Y., & Xing, Q. Y. (2024). Biomimetic anti-icing epoxy coating based on controlled-secreting hydrophobic small molecules in microcapsules through shrinkable gel under low temperature. *Colloids and Surfaces A: Physicochemical and Engineering Aspects, 691*, 133892.

[17] Yang, K., Wang, F., Shi, B., Zhang, Z., Feng, W., Qi, G., & Yan, H. (2025). Low-temperature curing epoxy self-lubricating anticorrosion coatings synergistically enhanced by hyperbranched polysiloxanes and MoS2/h-BN heterojunction particles. *Composites Part A: Applied Science and Manufacturing, 194*, 108920.

[18] Yu, M., Fan, C., Ge, F., Lu, Q., Wang, X., & Cui, Z. (2021). Anticorrosion behavior of organic offshore coating systems in UV, salt spray and low temperature alternation simulated Arctic offshore environment. *Materials Today Communications, 28*, 102545.

[19] Shibin, S. U. N., Changwei, S. H. I., Dongsheng, W. A. N. G., Xueting, C. H. A. N. G., & Mingchun, L. I. (2024). Low Temperature Wear and Corrosion Resistance of Epoxy Based Polar Marine Ice Breaking Coatings. *Journal of Chinese Society for Corrosion and Protection, 44*(5), 1177-1188.

[20] Sun, Y., Man, C., Kong, D., Cui, Z., Wang, X., Dong, C., & Cui, H. (2022). Correlation between low-temperature anticorrosion performance and mechanical properties of composite coatings reinforced by modified Fe3O4. *Progress in Organic Coatings, 165*, 106737.

[21] Arthanareeswari, M., Kamaraj, P., Tamilselvi, M., & Devikala, S. (2018). A low temperature nano TiO2 incorporated nano zinc phosphate coating on mild steel with enhanced corrosion resistance. *Materials Today: Proceedings, 5*(2), 9012-9025.

[22] Xie, Y., Chen, M., Xie, D., Zhong, L., & Zhang, X. (2017). A fast, low temperature zinc phosphate coating on steel accelerated by graphene oxide. *Corrosion Science, 128*, 1-8.

[23] Zhu, Q., Liu, J., Wang, X., Huang, Y., Ren, Y., Song, W., ... & Liu, C. (2020). Polypyrrole functionalized graphene oxide accelerated zinc phosphate coating under low-temperature. *ES Materials & Manufacturing, 9*(6), 48-54.

[24] Shi, B., Shen, X., Liang, G., Zhu, Y., & Xu, Q. (2022). The superhydrophobic coating with low-temperature dew point corrosion resistance on an acid-resistant steel substrate prepared by the electrodeposition method. *Materials and Corrosion, 73*(6), 903-917.

[25] Zhu, J., Pei, L., Yuan, S., Lin, D., Lu, R., Zhu, Y., & Wang, H. (2024). A unique graphene composite coating suitable for ultra-low temperature and thermal shock environments. *Progress in Organic Coatings, 186*, 107997.

[26] Zhang, P., Zhao, Y., Gu, X., Yang, K., Zhang, X., Liu, M., ... & Che, Y. (2024). Constructing carbon nanotube (CNTs)/silica superhydrophobic coating with multi-stage rough structure for long-term anti-corrosion and low-temperature anti-icing in the marine environment. *Composites Science and Technology, 257,* 110798.

[27] Zhu, G. K., Chen, H. Y., Fan, L., Han, L. L., Shen, Y. L., Cao, Q. Z., ... & Dong, L. H. (2024). Low-Temperature Corrosion Performance of Laser-Cladded Co-WB Coatings in Simulated Seawater. *Strength of Materials, 56*(1), 155-165.

[28] Wang, X., Fan, L., Xu, Y., Chen, H., Cao, Q., Dong, L., & Qin, Y. (2022). Low-temperature corrosion behavior of laser cladding metal-based alloy coatings on EH40 high-strength steel for icebreaker. *High Temperature Materials and Processes, 41*(1), 434-448.

[29] Kim, D. M., Cho, Y. J., Choi, J. Y., Kim, B. J., Jin, S. W., & Chung, C. M. (2017). Low-temperature self-healing of a microcapsule-type protective coating. *Materials, 10*(9), 1079.